Author/s:
Harley, WS;Kolesnik, K;Xu, M;Heath, DE;Collins, DJ

Title:
3D Acoustofluidics via Sub-Wavelength Micro-Resonators

Date:
2022-12-16

Citation:
Harley, W. S., Kolesnik, K., Xu, M., Heath, D. E. & Collins, D. J. (2022). 3D Acoustofluidics via Sub-Wavelength Micro-Resonators. Advanced Functional Materials, 33 (9), https://doi.org/10.1002/adfm.202211422.

Persistent Link:
https://hdl.handle.net/11343/332171

3D Acoustofluidics via Sub-Wavelength Micro-Resonators

*William Sean Harley, Kirill Kolesnik, Mingxin Xu, Daniel Edward Heath, and David John Collins**

Precise acoustic micromanipulation is emerging as an important tool in biomedical research, where acoustic forces have the advantage of being contact-free, label-free, and biocompatible. Conventional acoustofluidic approaches, however, produce device-scale effects that limit the ability to locally target acoustic energies at the microscale. In this study, we demonstrate an approach to generate designed and highly local acoustic fields using 3D resonant mass-spring microstructures, achieving local acoustic field gradients on the order of microns, orders of magnitude smaller than the fluid wavelength. In doing so, rapid and spatially defined controllable micromanipulation, including particle capture, transport, and patterning using arbitrarily arranged micro-resonator arrays is demonstrated. This sub-wavelength, 3D acoustofluidic approach results in highly localized and defined micromanipulation, with potential applications across sample preparation, cell analysis, and diagnostics.

1. Introduction

Microscale manipulation of particles, cells, and cellular aggregates is an essential technique in biomedical research with applications across single-cell analysis,[1,2] drug discovery,[3,4] and tissue engineering.[5,6] Micromanipulation methods such as optical tweezing, magnetophoresis, dielectrophoresis, and acoustophoresis.[7,8] Optical tweezers, for example, are unique in that they offer a very high degree of spatial resolution, with the ability to trap and transport individual cells and molecules. This technique, however, requires complex optics including lasers, high numerical aperture objectives, and can cause cell damage, with attraction toward regions of the highest optical intensity.[9,10] Electric fields similarly enable micro-manipulation by exposing cells to strong electric fields that drive particle and cell motion, although are similarly susceptible to cell damage at higher powers.[11,12] Magnetic fields have also found utility, although they are typically more limited in terms of their spatial selectivity, with fields permeating the bulk of the device, and where magnetophoresis often requires conjugated labels to perform manipulation.[13,14]

Acoustic fields, however, can utilize wavelengths that can approach the scale of individual cells[15,16] and are generally biocompatible, with the migration of particles and cells toward minimum acoustic energy positions,[17–19] making acoustofluidic devices a powerful tool for micromanipulation.[20–26] Owing to the tunable nature of acoustic waves and the wide range of operating frequencies used (kilohertz to gigahertz), acoustophoretic technologies can perform particle manipulation across length scales from sub-micron to millimeters.[27–29] Spatial selectivity has further been achieved via wavefield design approaches including acoustic holography,[30] focused transducers,[31,32] and pulsed actuation strategies,[33,34] although the scale of this selectivity is generally limited by the acoustic wavelengths utilized.

Acoustic-structure interactions, where acoustic fields diffract around or couple through patterned interfaces adjoining the transducers,[35–40] are also emerging as an area of interest, with the potential to generate yet more refined and localized actuation. Sub-wavelength features in particular are capable of generating evanescent acoustic effects whose gradients can be substantially smaller than the acoustic wavelength.[41–44] Acoustic streaming induced by vibrating sharp-edge microstructures, for instance, has been used for mixing,[45,46] propelling microrobots,[47,48] and nanoparticle concentration.[49,50] For instance, Lu et al. illustrated microstreaming-based traps for the parallel label-free cancer cell isolation in biological samples.[51] More recently, Rasouli et al. demonstrated the rapid formation of multicellular spheroids in a continuous flow using such acoustic streaming effects.[52] Utilizing a patterned cavity layer, Tayebi et al. further demonstrated the formation of microscale acoustic forces that captured individual 300 nm particles in 500 nm cavities. Together, this demonstrates the ability to effect microscale manipulation beyond the formation of periodic, wavelength-scale nodes and streaming vortices that are typical of standing wave acoustic devices.[53–56] While a variety of microstructures have been thus used to generate microstreaming and acoustic radiation effects, these have been constrained in terms of their

W. S. Harley, K. Kolesnik, M. Xu, D. E. Heath, D. J. Collins
Department of Biomedical Engineering
University of Melbourne
Melbourne, VIC 3010, Australia
E-mail: david.collins@unimelb.edu.au

W. S. Harley
Micro Nano Research Facility
RMIT University
Melbourne, VIC 3000, Australia

D. J. Collins
The Graeme Clark Institute
The University of Melbourne
Parkville, VIC 3052, Australia

The ORCID identification number(s) for the author(s) of this article can be found under https://doi.org/10.1002/adfm.202211422.

DOI: 10.1002/adfm.202211422

versatility (with limited ability to determine arbitrary arrangements and define complex acoustic fields in 3D) and their performance (where structural oscillations are constrained by unoptimized, simple geometries which limit their actuation distance in height). For instance, while acoustic fields are intrinsically 3D, planar acoustic devices typically produce periodic effects with systemic, rather than local and defined effects. While evanescent fields from periodic cavity structures have shown the ability for sub-wavelength cavities to generate evanescent fields on similar scales,[50] the location, arrangement, and vertical scale of these fields are limited. These limitations ultimately arise from the dimensionality of the structures and fabrication methods employed, being typically planar and layer-by-layer, respectively.

In this work, we demonstrate 3D acoustofluidic micro-resonators for targeted micromanipulation, in which microfabricated and optimized spring-mass systems generate large displacements and thus rapid microfluidic actuation. An example of an acoustically resonant structure in the natural world is the basilar membrane in the ear, enabling the frequency-selective magnification of acoustic displacements. In this work a micro-resonator structure similarly enhances and magnifies acoustic oscillations, enabling on-demand micromanipulation via ultrasonic streaming and acoustic radiation forces, here utilizing actuation of microprinted 3D microstructures via a 7 MHz, bulk acoustic wave (BAW) transducer. The structures are fabricated via 3D microprinting, yielding complex geometries whose dimensions can be tailored for optimal acoustic excitation. The oscillation of these sub-wavelength, ≈10 µm scale structures produce highly localized evanescent acoustofluidic fields that can be used to focus and manipulate microscale objects.

To generate maximum displacements in these micro-resonators, numerical modeling is used to optimize their dimensions for a given actuation frequency. This modeling is validated experimentally, showing enhanced actuation for a range of microstructure geometries, with resulting particle interactions yielding local rotational and aggregation activities. Further, as these elements can be arbitrarily patterned across a microfluidic domain, the concerted action of these structures can be coordinated to produce designed micropatterning across large areas, essentially converting planar acoustic excitation into designed configurations, yielding unique arrangements that would not be feasible using conventional acoustofluidic actuation. Finally, we demonstrate a range of micro-resonator device geometries, exhibiting the flexibility of this approach in determining the orientation and morphology of the local acoustic field, and thus the preferred location(s) at which microparticles interact. The ability to generate high-magnitude, sub-wavelength acoustic fields via 3D acoustofluidic micro-resonators is thus an enabling approach that significantly expands the versatility and performance of acoustofluidic micromanipulation.

2. Concept and Operating Principles

Figure 1 depicts the micro-resonator device concept, where 3D structures are embedded inside a microfluidic polydimethylsiloxane (PDMS) chamber on fused silica. Acoustic energies are coupled to the silica substrate via a thin layer of water from piezoelectric $LiNbO_3$ crystal coated with uniform conductive chromium/aluminum electrode layers. When the piezoelectric transducer is actuated with an alternating current electrical input, it generates a bulk-mode resonance along the transducer thickness (z-axis), where mechanical displacements are coupled through to the silica layer to induce vibration in 3D micro-resonators. Such a superstrate-based approach, where the microfluidic component is not directly bonded to the transducer, makes the microfluidic component interchangeable and simplifies microchannel bonding. The induced particle manipulation effected by these micro-resonators is influenced by the combined influences of acoustic radiation forces and acoustically induced flow, the latter termed acoustic streaming.[57] The latter, acoustic streaming, results from the attenuation and transfer of acoustic energy into bulk fluid motion and influences particle motion by generating fluid flow.[58]

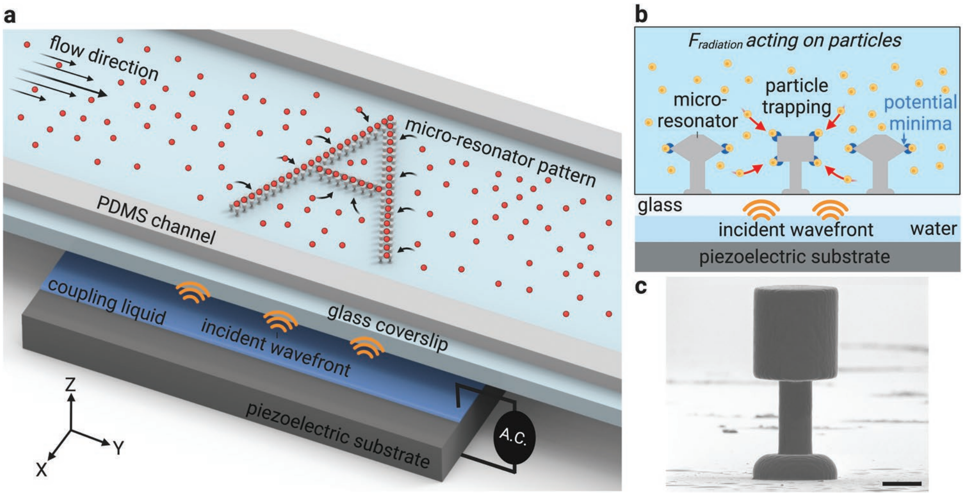

Figure 1. 3D acoustofluidic micro-resonator concept. a) Microfluidic device schematic incorporating 3D acoustofluidic micro-resonators, where these are contained inside a microfluidic chamber bounded by polydimethylsiloxane (PDMS) and fused silica. Piezoelectric actuation is coupled from the transducer to the microfluidic device via a thin fluid coupling layer. b) Side view illustrating particle trapping behavior around spring-mass resonators, with a concentration in the vicinity of sharp edges. c) Helium ion microscopy (HIM) image of a representative 3D micro-resonator structure. Scale bar is 5 µm (the acoustic wavelength in water at 7 MHz is 213 µm).

Whereas both acoustic radiation forces and acoustic streaming are both periodic and wavelength-scale in conventional acoustofluidic systems, including those driven by BAW[59] and surface acoustic wave[60] actuation, the use of resonant 3D sub-wavelength microstructures here enables the generation of highly localized, sub-wavelength acoustofluidic effects. This principle is shown in Figure 1b, where suspended particles translate along acoustic force potential gradients, from regions of high acoustic potential to lower ones. The acoustic force potential is calculated using a combination of the first-order pressure and velocity fields; as higher velocities result in lower potentials, and the highest first-order velocities are generated in the vicinity of sharp boundaries, particles are generally attracted toward micro-resonator edges. An example microfabricated 'mushroom cap' resonator image is shown in Figure 1c.

3. Results and Discussion

3.1. Numerical Modeling

To map the acoustic potential distribution around microstructures, as well as to understand the impact of resonator dimensions on performance, an isolated micro-resonator structure is simulated in an axisymmetric (radially symmetric) study (Figure S1a, Supporting Information) within a simulated microfluidic environment. The bottom boundary has a prescribed uniform velocity actuation of 1 m s^{-1} which produces a pressure wave propagating upward and partly reflecting from the PDMS boundary atop the 100 µm high microfluidic chamber. **Figure 2**a plots the resulting pressure amplitude in the fluid domain from a structure whose mass component has a diameter of 10 µm and is 10 µm high, with a displacement from the transducer surface of 12 µm; this figure focuses on the acoustic field in the immediate vicinity of the micro-resonator. As the actuated micropillar experiences mechanical resonance, this yields a 4.5 times higher displacement (at the structure's top surface) compared to the actuation amplitude. This figure shows that the oscillating structure generates an evanescent field with a pressure minima on top, and with a pressure maxima along the bottom surface. Figure 2b further plots the velocity magnitude, with peak values near both the top and bottom surfaces.

Rather than being a function of either the velocity or pressure field alone, however, acoustophoretic focusing is governed by the acoustic potential field, which is a function of both pressure and velocity, and where particles are directed toward acoustic potential minima. The potential U^{rad} is the sum of the monopole $U^{\mathrm{rad}}_{\mathrm{mp}}$ and dipole $U^{\mathrm{rad}}_{\mathrm{dp}}$ terms,which depend on

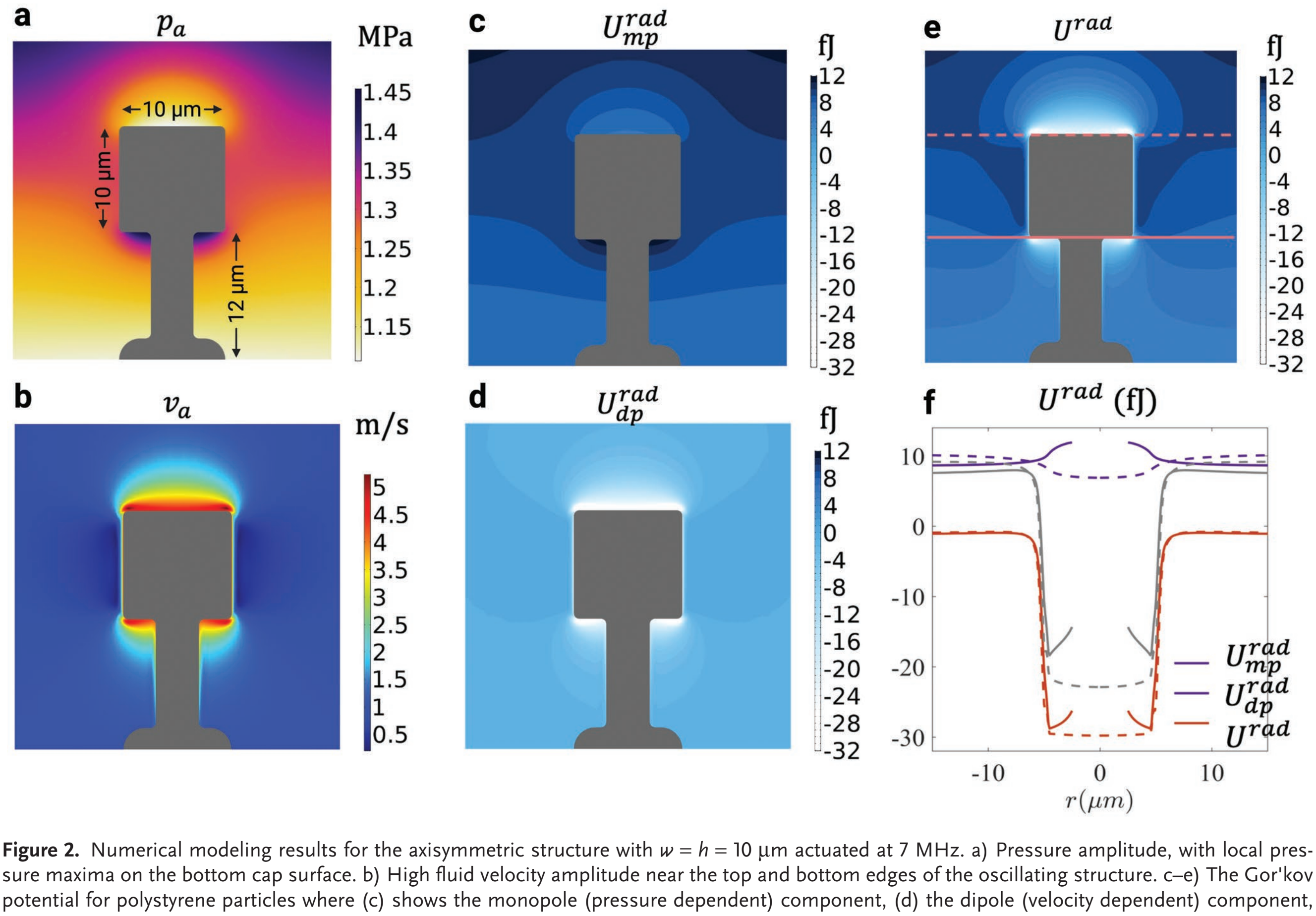

Figure 2. Numerical modeling results for the axisymmetric structure with $w = h = 10$ µm actuated at 7 MHz. a) Pressure amplitude, with local pressure maxima on the bottom cap surface. b) High fluid velocity amplitude near the top and bottom edges of the oscillating structure. c–e) The Gor'kov potential for polystyrene particles where (c) shows the monopole (pressure dependent) component, (d) the dipole (velocity dependent) component, and (e) resulting combined potential field with minima near the top and bottom of both cap surfaces. f) Plot highlighting the differences between pressure-dependent monopole and velocity-dependent dipole components against the resulting potential field at the top (dotted) and bottom (solid line) of the microstructure shown in (e).

the local time-averaged complex-valued pressure $\langle p^2 \rangle$ and velocity $\langle \mathbf{v}^2 \rangle$ fields, respectively, and which is examined in Equation (17) (Experimental Section). Whereas the pressure and velocity distribution are intrinsic to the fluidic domain in the vicinity of a structure, the potential distribution is a function of a particle's interaction with these fields, where the results in Figure 2c–f are plotted for a representative 3 µm polystyrene particle. The monopole term distribution (Figure 2c) is determined by the pressure amplitude and thus reaches its local minima near the pillar and top and bottom boundaries of the domain. The dipole term (Figure 2d), in turn, reaches its minimum near the top and bottom interfaces where the acoustic velocity has its highest value. As the dipole component is of substantially greater magnitude than that of the monopole one, the resulting Gor'kov potential U^{rad} (Figure 2e,f) has a minimum near both top and bottom surfaces, where Figure 2f plots U^{rad} along the cross sections along the top (dashed line) and bottom (solid line). As the minima appear along these interfaces, these are the locations that particles are expected to preferentially aggregate. Movie S1 (Supporting Information) visualizes the time-dependent fluid velocity field near the pillar and the continuum displacements (amplitudes 5x upscaled for visualization purposes) over one oscillation period.

3.2. Parametric Analysis

To understand the relationship between microstructure configuration and resulting acoustic field, a parametric study was conducted examining microstructure dimensions. In the parametric sweep, the mass ('cap') width *w* and height *h* were varied between 5 to 15 µm, using a constant actuation frequency of 7 MHz (this being the native bulk-mode resonant frequency of the 0.5 mm thick $LiNbO_3$ transducer).[61] The acoustic potential contrast for this parameter space is plotted in **Figure 3**a, where this contrast value is determined via Equation (18) (see Experimental Section) and is a measure of the acoustic potential field gradient in the vicinity of a given microstructure. The configurations with high contrast values are predicted to demonstrate efficient particle focusing near the cap due to larger acoustophoretic forces. This figure delineates ideal combinations of cap width and height, where a higher *w* corresponds to lower *h* to achieve a high-contrast acoustic field. This behavior can be understood as that of a mass attached to a spring; For a given spring constant and actuation frequency, structures will resonate for a given mass value, explaining the viability of multiple optimal configurations to generate resonance conditions, as the mass of the cap component is conserved across this range. Taller configurations (small *w*) appear to show somewhat

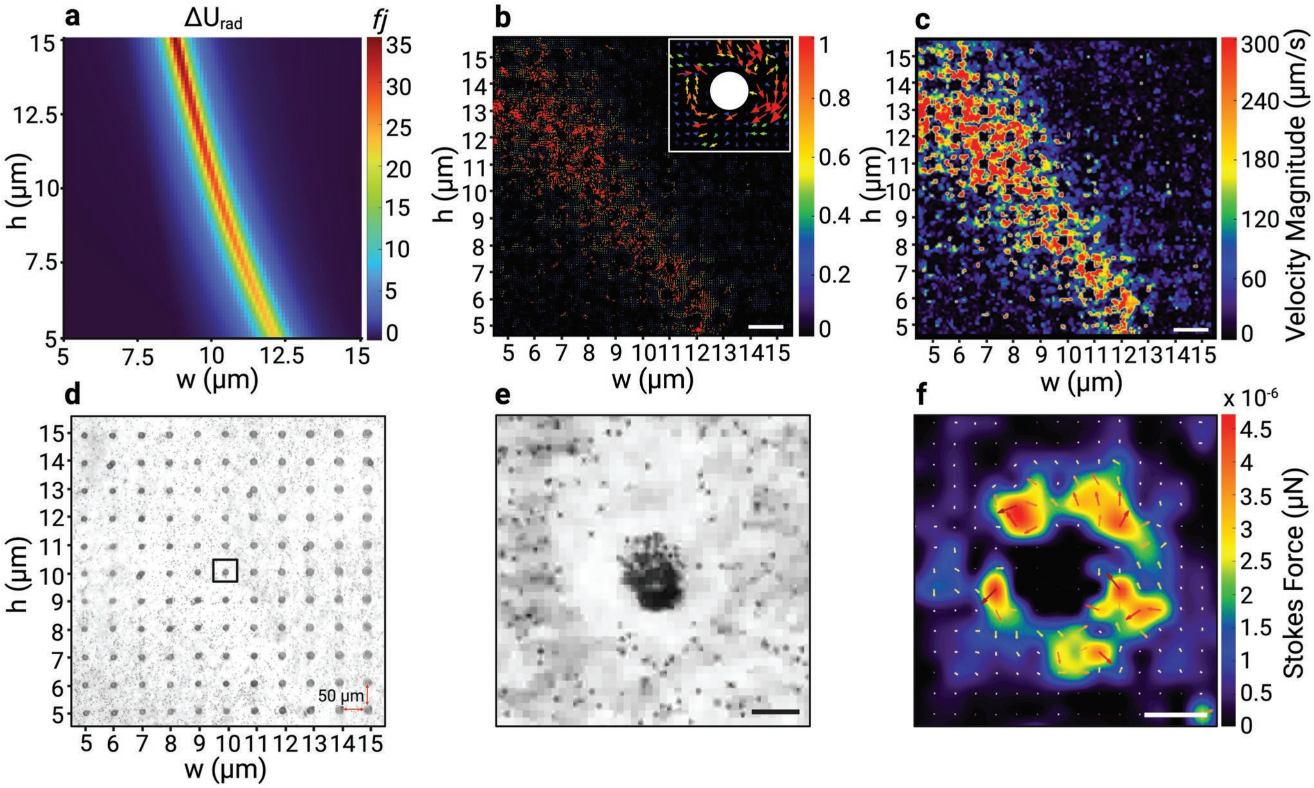

Figure 3. Parametric micro-resonator examination. a) Numerical parametric study where the Gor'kov potential contrast (Equation (18)) is calculated in the vicinity of caps with different *w* and *h*. High contrast configurations correspond to mechanical resonance. Colorbar has units of femtojoules. PIV analysis using 1 µm fluorescently labeled particles in a microstructure array whose cap dimensions correspond to the axes given. Scale bars are 100 µm. The image in b) displays a vector plot with inset highlighting rotation around a single microstructure, and c) shows the velocity magnitude map. These are obtained using a d) array design with 50 µm interval spacings. The image in e) highlights a selected *w* = 10, *h* = 10 µm microstructure configuration showing particle focusing. Results in f) show a contour map of the drag force for a 1 µm particle superimposed with arrows indicating the magnitude and direction of fluid flow. Scale bars are 10 µm.

higher contrast, due to reduced viscous damping with a smaller cross section, albeit at the expense of frequency selectivity, higher aspect ratios, and a greater distance between the top and bottom patterning areas of the cap.

While such numerical modeling is useful for exploring such parameter spaces in fine detail, this has limitations, however, in terms of representing non-axisymmetric oscillation modes that arise in an actual device. First, we consider the primary resonance mode to be longitudinal due to the predominately vertical displacement of the piezoelectric substrate, which is actuated as a bulk-mode resonator; other modes (e.g., bending) would be more likely in the case of transducer displacements with an out of plane component. Further, in this work we assess the acoustic field as a function of device geometry, where specific combinations of structure dimensions are required to produce longitudinal mode resonance for a given frequency; given the sensitivity of resonance to structure dimensions, the excitation of other resonance modes would be maximally affected at other frequencies than the 7 MHz one used here. These other oscillation modes may be generated by secondary flexural waves in the substrate due to clamping and device positioning, a non-even coupling layer, whole channel/chip resonances, and impact of the neighboring microstructures. Moreover, volumetric flows can impact particle positioning, and in addition, as a point scattering model was used (where this allows fine-grained examination of the evanescent field), the numerical model doesn't consider interparticle interactions. To validate our numerical modeling and evaluate resonance behavior in an experimental setting, an equivalent parameter space was explored in an array of microstructures, with Figure 3b–f examining the results from these. In this array, the same width and height ranges are explored, with 11 discrete values of each (i.e., $h = 5$ µm, 6 µm, 15 µm, $w = 5$ µm, 6 µm, 15 µm) and the combination of each, for a total of 121 micro-resonator structures. To evaluate their behavior, particle image velocimetry (PIV) was conducted with 1 µm particles, showing the particle motion in the structure's vicinity; here the acoustic streaming magnitude is used as a proxy for the acoustic force potential field, with stronger streaming corresponding to larger displacements,[62] with the caveat that off-target resonance modes (i.e., rotational ones) may preferentially yield streaming at different frequencies/dimensions compared to the primary (vertical) one.

Nevertheless, we observe similar trends for geometries producing particle actuation between the simulation and experimental results. Figure 3b displays the particle trajectory vector plot for this array, with the inset showing rotation behavior around a single microstructure. Figure 3c plots the total velocity magnitude (in µm/s) as well, demonstrating rapid actuation on the order of 100's of microns per second. Both plots demonstrate a range of combinations for w and h that yield enhanced particle manipulation velocities, analogous to the numerical modeling results, albeit somewhat offset for taller/thinner structures. These PIV studies were conducted using the design layout shown in Figure 3d, where a range of structures with cap widths w and heights h are spaced 50 µm apart, yielding a wide range of structures that can be viewed in a single image frame while simultaneously being able to visualize individual 1 µm particle trajectories. Figure 3e,f highlights a magnified image of a representative structure demonstrating particle focusing and the corresponding drag force map, whereas Figure 3f shows a contour map of the drag force for a 1 µm particle superimposed with arrows indicating the magnitude and direction of fluid flow. Although the vectors here do not necessarily point in a perfectly circular orbit around the structure, we note that the image is captured in 2D, whereas fluid motion around this 3D structure, and therefore also the particles being tracked, occurs in three-dimensions. This structure corresponds to a 10 µm high, 10 µm wide cap, examined here as it is within both the left and right edges of the numerical and experimental domains, respectively, and exhibits effective particle manipulation.

3.3. Single Structure Microstreaming

The ultrasonic microstreaming fields around individual structures are analyzed by arranging 100 uniform 3D micro-resonators into a 100 µm evenly spaced array, with a total area covering 1 mm^2. Arranging each of these 10 µm diameter structures with this spacing allows us to observe singular particle micromanipulation while avoiding avoid interference from neighboring structures. The same frequency used in the numerical modeling was also the one applied to the transducers in the microfluidic device. This 7 MHz frequency is further observed to elicit the strongest acoustophoretic response in this fabricated array, in accordance with the simulation results. As predicted by numerical modeling, the experimental analysis also demonstrates that suspended particles migrate toward the acoustic potential minima at the cap interfaces, further exhibiting ring-shaped particle rotation due with axial symmetry of the mushroom cap structures. As shown in **Figure 4**a, the acoustic streaming flow field is observed at the cap interface where both 10 µm particles (top) and 3 µm particles (bottom) are subject to particle focusing and rotation around the structure's edges. As the 3 µm particles are substantially smaller than the distance between the substrate and the lower cap surface, aggregation occurs on both the top and underneath, compared to larger particles which are sterically inhibited from being fully captured on the underside.

Particle tracking is realized by implementing a velocimetry tool,[63] where Figure 4b plots the trajectory for a 10 µm particle overlaid over a contour plot of the theta velocity magnitude. Attraction is observed to commence approximately ≈30 µm from the cap's center (with velocities on the order of ≈1–10 µm s^{-1}). At or around 20 µm from the center of the pillar structure, however, velocity magnitudes increase rapidly from 10–30 µm s^{-1} to up to 150 µm s^{-1} as the particle reaches the resonator edges. The inset in Figure 4b illustrates a superimposed image sequence of this attraction process. This data is captured and analyzed across 200 frames. Plots displayed in Figure 4c,d examine the total velocity magnitude and the radial velocity magnitude in more detail, each with respect to the distance between the center point of the resonator and particle, demonstrating the rapid and highly local actuation that occurs in the vicinity of each microstructure. Figure 4d further shows agreement between the trend of the numerical simulation result (red line) and experimental measurements (black dots), where attraction speed is proportional to the applied acoustic force.

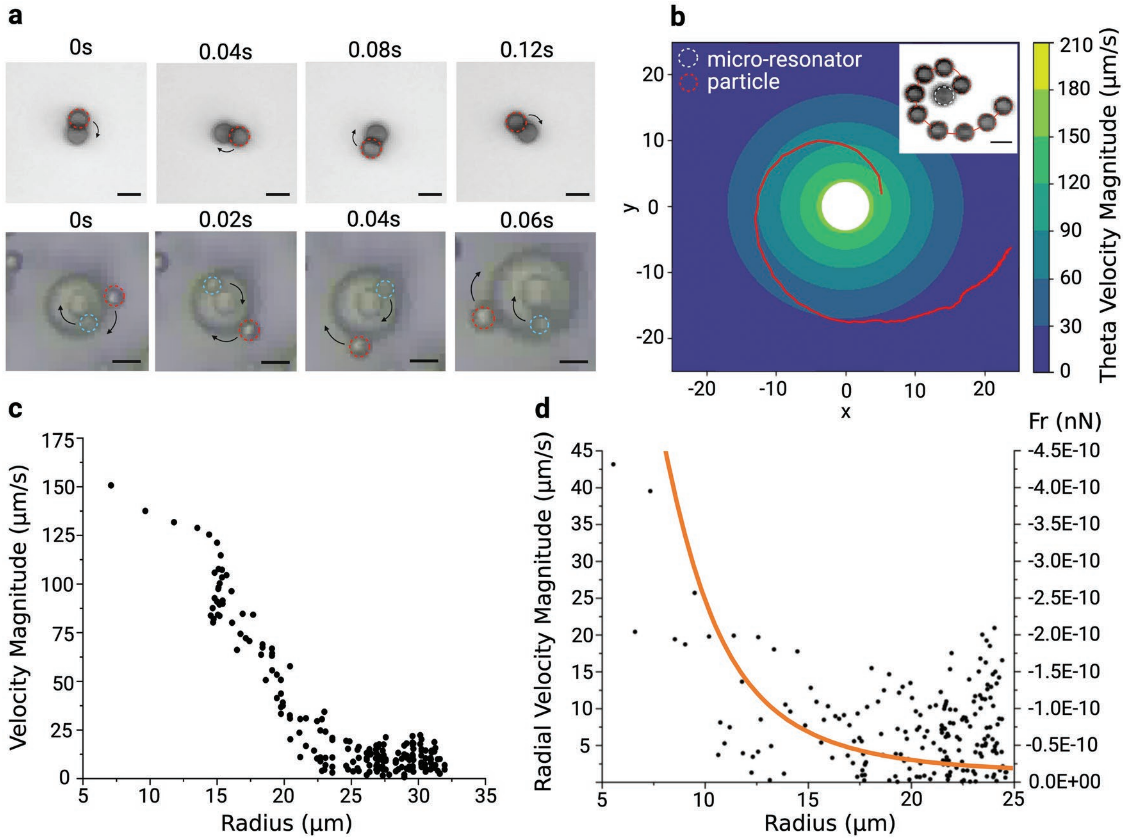

Figure 4. Rotational motion and aggregation around a single micro-resonator. a) Optical brightfield microscopy images capturing time-dependent rotation of (top) 10 µm (bottom) 3 µm particles around a single. Scale bars are 10 and 5 µm, respectively. b) Particle tracking of a single 10 µm particle, with the theta velocity magnitude, is expressed as a radial contour plot overlayed with the 10 µm particle trajectory expressed as x, y coordinates. c) Absolute velocity magnitude, where radius represents the distance between centers of the microstructure and particle. d) Radial velocity magnitude overlaid with the acoustic force calculated from the simulations, with $F = \nabla U^{\mathrm{rad}}$.

3.4. Multiplexed Patterning and Complex Arrangements

In addition to manipulation around individual microstructures, complex transport and the generation of coordinated assemblies in non-uniform patterns is also desirable.[64] To demonstrate this capability, and in line with the concept diagram in Figure 1a, we show in **Figure 5**a the aggregation of 3 µm fluorescently labeled green particles that occurs when micro-resonators are arrayed in the shape of the letter ‘A’, where these particles are drawn from the surrounding suspension toward these microstructures. Figure 5b–e further demonstrates examples of non-uniform patterns and alternative arbitrary arrangements, illustrating the versatility of this approach. Figure 5b shows an arrangement in the shape of our lab logo, Figure 5d shows a uniform grid, and Figure 5c,e shows circular resonator configurations. Each of the images in Figure 5 is captured from a single frame at the timepoint shortly after the application of the acoustic field, with Movie S2 (Supporting Information) (corresponding to Figure 5e) showing an example of this aggregation behavior. The top right of Fig. 5e highlights an example of the initial particle distribution for a given section of this array. Figure 5e in particular explores the effects of circular structure arrangements with different angular spacings, indeed where these structures are immediately neighboring one another along the left of this image. As the resonance behavior ad particle attraction is driven by their vertical oscillation, the acoustic force potential gradients drawing particles toward them are not impacted by the horizontal co-localization of additional microstructures, even when they are immediately next to one another. In this case, particles can be seen to be drawn from inside these circular arrangements to the microstructure locations along the circumference, clearing their interiors (white arrows in Figure 5e). Movie S3 (Supporting Information) further evidences particle capture in the array from Figure 5b, here with a flow applied until the array is filled.

3.5. Alternative Resonator Geometries

Whereas these ‘mushroom’ shaped structures demonstrated in previous sections are a straightforward implementation of a spring-mass resonator geometry, the ability to arbitrarily define the 3D geometry of such structures permits the acoustic field to be further locally designed and tailored as well. Evidencing this, we further numerically model and test alternative geometries in **Figure 6**, in which the number and shape of acoustic force potential minima (and thus particle aggregation locations)

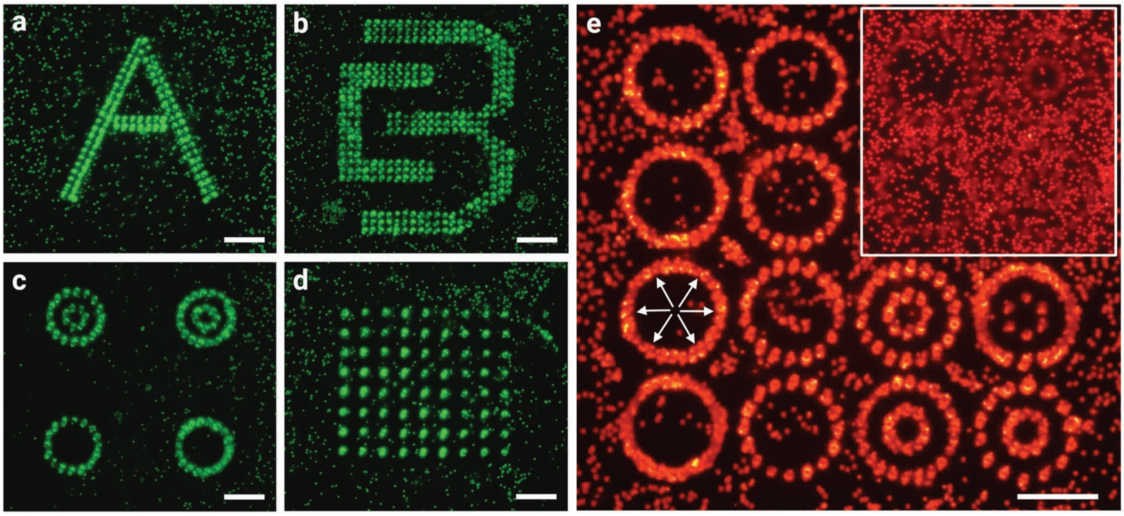

Figure 5. Microparticle patterning in arbitrary arrangements via patterned micro-resonators. Here with a) denoting the letter 'A', b) Collins BioMicrosystems Laboratory (CBML) logo, c) circular patterns, d) a rectilinear array, and e) variations of concentric circles with different angular spacings. Scale bars are 100 µm.

is varied by changing the location of edge features and/or symmetry of the resonator. Examples of alternative resonators are all geometrically optimized for resonance at 7 MHz, the native-bulk mode actuation resonance of the $LiNbO_3$ transducer. These structures include a biconical structure with a single ring-shaped sharp edge (first row) with cap dimensions of $h = 22$ µm and $w = 11$ µm, an asymmetric mass with a $h = 22$ µm and a cap $w = 6$ µm intended to exhibit a lateral (rather than vertical) resonance mode (second row) and a modification of the microstructure shown in Figures 2–5 with a cap $h = 8$ µm *and* $w = 21$ µm in which the sharpness of the edges on the top and bottom are highly accentuated (third row). The potential fields for each are shown in Figure 6a–c, Figure 6d–f shows HIM images, and Figure 6g–i displays experimental results with 3 µm microparticles. For the case of the structures in the second and third row, their geometry permits them to be extruded to arbitrary lengths, with the experimental images evidencing examples of linear resonant structures (viewed from the top). Annotations highlighted on these images indicate the observed manipulation direction, including rotation around a single structure, aligned transport along an elongated structure, and particle aggregation in a streaming-enhanced cluster. For the structures in the first and second row, the aggregation location(s) accords with the acoustic potential minima given in Figure 6a,b, with particles being attracted to the edges of the conical structure in Figure 6g and on the top two corners around the cylindrical extension in Figure 6h. Particle motion in Figure 6i, however, appears to be increasingly dominated by acoustic streaming, where sharper edge structures preferentially generate more rapid flows compared to less angled features.[65,66]

4. Conclusion

In this work, we generate highly localized evanescent acoustic fields via micro-resonator structures. Despite the utilization of an acoustic field whose fluidic wavelength of 100's of microns, this yields acoustic field gradients orders of magnitude smaller, permitting sub-wavelength actuation and trapping. This is enabled by unique 3D microfabricated resonator geometries in which microfabricated spring-mass systems generate amplified displacements, producing rapid and local actuation. Their design further generates displacements that are a multiple of the transducer amplitude, magnifying and localizing acoustic energies. Compared to acoustic approaches that rely on the acoustic field permeating an entire device, and in which the patterning effects are periodic, this resonator approach permits highly defined and localized actuation.

We have accordingly demonstrated on-demand rotation and microparticle patterning into complex arbitrary arrangements, where simulations show the acoustic field morphologies in the vicinity of microstructures. This method also highlights the versatility of microprinted 3D geometries to produce defined 3D acoustic fields. Whereas the bulk of acoustic work is predicated on planar transducers and interfaces produced via 2D fabrication methods, generating acoustic fields that are defined in a given plane, this work yields complex acoustic fields from 3D geometries whose dimensions can be tailored for optimized acoustic excitation. This is both in terms of the acoustic field surrounding each structure as well as device-scale micro-resonator arrangements. This work thus represents an important step in generating highly localized acoustic micromanipulation, where cell-scale manipulation has applications in capturing single cells for mechanical analysis,[67] precise handling of droplets for drug discovery,[68] and the coordinated patterning of cells for tissue engineering.[69]

5. Experimental Section

Waveguide Fabrication: 3D micro-resonators were designed using CAD software (Solid Edge 2021, Siemens) and prepared using DeScribe software (Nanoscribe, GmbH). The Photonic Professional GT2, a

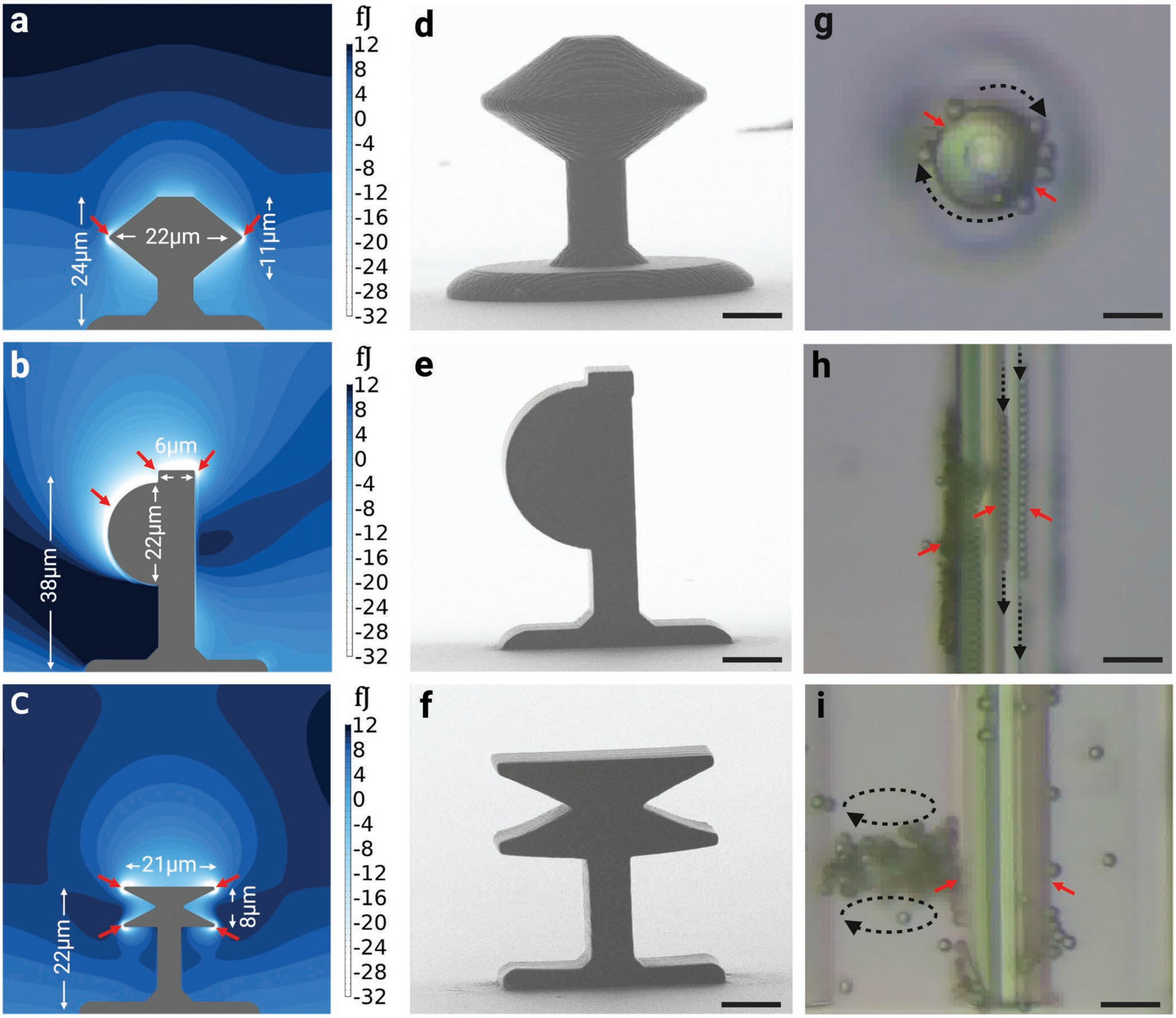

Figure 6. Examples of different resonator geometries. a–c) Numerical modeling results for structures actuated at 7 MHz and the resulting potential field, with minima denoting locations to which particles aggregate. d–f) Representative HIM images of the fabricated devices and their cross sections. Scale bars are 5 µm. g–i) Experimental brightfield images illustrating particle manipulation behavior. Red arrows show the region(s) where the force potential gradient is maximized in both the simulation and experimental images, and black arrows indicate directional particle motion. Scale bars are 10 µm.

two-photon polymerization nanoscale 3D printing system by (Nanoscribe, GmbH), was employed to print the designed polymeric microstructures. A femtosecond pulsed laser with 100 fs pulse duration, 80 MHz repetition rate, and 780 nm wavelength was focused into the liquid negative photoresist IP-Dip2 by an immersion objective lens (63x, NA = 0.8, WD = 200 µm), where the structures were fabricated on a 0.5 mm thick fused silica substrate. Two-photon polymerization occurs at the focal point of the beam, where this beam position is scanned rapidly by galvanometric mirrors in the XY plane, while its Z position was determined by a piezoelectric translation stage to achieve resist cross-linking in three dimensions. For the exposures, the laser power was 40 mW, beam scan speed 100 mm s^{-1}, vertical slicing distance 0.2 µm, and in-plane hatching distance of 0.2 µm. After laser writing, samples were developed in polyethylene glycol methyl ether acetate (50 mL) for 5 min to remove unexposed photoresist, followed by immersion in isopropyl alcohol (50 mL) for 5 min. Finally, the printed microstructures were subject to gentle N_2 blow drying and left to dry at room temperature.

Experimental Setup: The microfluidic device consisted of a microfluidic channel bonded to a piece of fused silica, which was coupled by a thin layer of water to a piezoelectric transducer. The microfluidic cavity enclosing these microstructures was fabricated using a standard PDMS soft-lithography process (prepolymer to curing agent weight ratio at 10:1, Sylgard 184 Silicone Elastomer Kit, Dow corning Corp), in which the master mold for PDMS casting was fabricated with SU-8 (SU-8 3050, MicroChem, Newton, MA, USA) on a silicon wafer. The microfluidic cavity was a square 6 mm^2 with a height of 100 µm with a single inlet and outlet. The prefabricated waveguides on the fused silica substrate, together with the PDMS microchannel layer, were treated under air plasma (Plasma Etch, PE-50, NV, USA) to generate hydroxyl functional groups on the surfaces. The treated surfaces were brought into contact and aligned to form a closed microfluidic channel.

The piezoelectric transducer was actuated using sinusoidal signals from a function generator (Tektronix AFG3102C, Beaverton, USA) through an amplifier (Mini-Circuits TVA-R5-13A+, USA). Particle suspensions were injected into the microfluidic device via a syringe pump (Harvard apparatus, MA, USA) at a flow rate of 30 µL min^{-1}, with flow stopped immediately prior to actuation, with the outlet being temporarily sealed to isolate the observation of particle motion in the absence of background flow. The observation was conducted using a fluorescence microscope (Olympus BX51, Japan) with a CCD camera (AmScope, CA, USA).

Microparticles that were used to demonstrate coordinated manipulation were 1, 3, and 10 µm, green, red, and blue, fluorescent polystyrene microspheres (Magsphere Inc., Pasadena, CA, USA). These particles were suspended in deionized water, containing 1% (w/v) Pluronic F127 (Sigma–Aldrich, USA) in concentrations ranging from 20–60 µL mL^{-1} to avoid particle agglomeration and adhesion onto the microfluidic channel walls. The particle suspension is then placed in an ultrasonic cleaner (Elmasonic P60 series, Elma, Germany) for 4 min at 37 kHz to facilitate bubble dissipation prior to infusing into the microfluidic device.

Numerical Simulation: See Supporting Information Note S1.

Supporting Information

Supporting Information is available from the Wiley Online Library or from the author.

Acknowledgements

This work was performed in part at the Melbourne Centre for Nanofabrication (MCN), RMIT Micro Nano Research Facility (MNRF), Materials Characterisation and Fabrication Platform (MCFP) at the University of Melbourne and the Victorian Node of the Australian National Fabrication Facility (ANFF). D.J.C. is the recipient of a Discovery Early Career Researcher Award from the Australian Research Council (DECRA, DE200100909), and funding from the National Health and Medical Research Council (Ideas, APP2003446). Selected figures were created with BioRender.com

Open access publishing facilitated by The University of Melbourne, as part of the Wiley - The University of Melbourne agreement via the Council of Australian University Librarians.

Conflict of Interest

The authors declare no conflict of interest.

Data Availability Statement

The data that support the findings of this study are available in the supplementary material of this article.

Keywords

3D printing, acoustofluidics, microfluidics, micromanipulations, micro-resonators

Received: October 2, 2022
Revised: November 23, 2022

[1] D. J. Collins, B. Morahan, J. Garcia-Bustos, C. Doerig, M. Plebanski, A. Neild, *Nat. Commun.* **2015**, *6*, 8686.
[2] V. Romanov, G. Silvani, H. Zhu, C. D. Cox, B. Martinac, *Small* **2021**, *17*, e2005759.
[3] P. Neuzi, S. Giselbrecht, K. Lange, T. J. Huang, A. Manz, *Nat Rev Drug Discov* **2012**, *11*, 620.
[4] G. Schneider, *Nat. Rev. Drug Discovery* **2018**, *17*, 97.
[5] W. S. Harley, C. C. Li, J. Toombs, C. D. O'Connell, H. K. Taylor, D. E. Heath, D. J. Collins, *Bioprinting* **2021**, *23*, e00147.
[6] B. Kang, J. Shin, H. J. Park, C. Rhyou, D. Kang, S. J. Lee, Y. S. Yoon, S. W. Cho, H. Lee, *Nat. Commun.* **2018**, *9*, 5402.
[7] H. Yun, K. Kim, W. G. Lee, *Biofabrication* **2013**, *5*, 022001.
[8] E. K. Sackmann, A. L. Fulton, D. J. Beebe, *Nature* **2014**, *507*, 181.
[9] H. Zhang, K. K. Liu, *J R Soc Interface* **2008**, *5*, 671.
[10] G. R. Kirkham, E. Britchford, T. Upton, J. Ware, G. M. Gibson, Y. Devaud, M. Ehrbar, M. Padgett, S. Allen, L. D. Buttery, K. Shakesheff, *Sci. Rep.* **2015**, *5*, 8577.
[11] C. Qian, H. Huang, L. Chen, X. Li, Z. Ge, T. Chen, Z. Yang, L. Sun, *Int. J. Mol. Sci.* **2014**, *15*, 18281.
[12] T. K. Chiu, W. P. Chou, S. B. Huang, H. M. Wang, Y. C. Lin, C. H. Hsieh, M. H. Wu, *Sci. Rep.* **2016**, *6*, 32851.
[13] A. Tocchio, N. G. Durmus, K. Sridhar, V. Mani, B. Coskun, R. El Assal, U. Demirci, *Adv. Mater.* **2018**, *30*, 1705034.
[14] V. A. Parfenov, Y. D. Khesuani, S. V. Petrov, P. A. Karalkin, E. V. Koudan, E. K. Nezhurina, F. D. Pereira, A. A. Krokhmal, A. A. Gryadunova, E. A. Bulanova, I. V. Vakhrushev, I. I. Babichenko, V. Kasyanov, O. F. Petrov, M. M. Vasiliev, K. Brakke, S. I. Belousov, T. E. Grigoriev, E. O. Osidak, E. I. Rossiyskaya, L. B. Buravkova, O. D. Kononenko, U. Demirci, V. A. Mironov, *Sci. Adv.* **2020**, *6*, eaba4174.
[15] M. Wu, A. Ozcelik, J. Rufo, Z. Wang, R. Fang, *T. Jun Huang, Microsyst Nanoeng* **2019**, *5*, 32.
[16] M. Tayebi, D. Yang, D. J. Collins, Y. Ai, *Nano Lett.* **2021**, *21*, 6835.
[17] J. P. K. Armstrong, J. L. Puetzer, A. Serio, A. G. Guex, M. Kapnisi, A. Breant, Y. Zong, V. Assal, S. C. Skaalure, O. King, T. Murty, C. Meinert, A. C. Franklin, P. G. Bassindale, M. K. Nichols, C. M. Terracciano, D. W. Hutmacher, B. W. Drinkwater, T. J. Klein, A. W. Perriman, M. M. Stevens, *Adv. Mater.* **2018**, *30*, 1802649.
[18] S. Cohen, H. Sazan, A. Kenigsberg, H. Schori, S. Piperno, H. Shpaisman, O. Shefi, *Sci. Rep.* **2020**, *10*, 4932.
[19] C. Devendran, K. Choi, J. Han, Y. Ai, A. Neild, D. J. Collins, *Lab Chip* **2020**, *20*, 2674.
[20] J. Rufo, P. Zhang, R. Zhong, L. P. Lee, T. J. Huang, *Nat. Commun.* **2022**, *13*, 3459.
[21] A. Fakhfouri, C. Devendran, T. Albrecht, D. J. Collins, A. Winkler, H. Schmidt, A. Neild, *Lab Chip* **2018**, *18*, 2214.
[22] D. J. Collins, R. O'Rorke, C. Devendran, Z. Ma, J. Han, A. Neild, Y. Ai, *Phys. Rev. Lett.* **2018**, *120*, 074502.
[23] F. Akkoyun, S. Gucluer, A. Ozcelik, *Biomicrofluidics* **2021**, *15*, 061301.
[24] K. Dholakia, B. W. Drinkwater, M. Ritsch-Marte, *Nat. Rev. Phys.* **2020**, *2*, 480.
[25] E. Undvall Anand, C. Magnusson, A. Lenshof, Y. Ceder, H. Lilja, T. Laurell, *Anal. Chem.* **2021**, *93*, 17076.
[26] A. Link, J. S. McGrath, M. Zaimagaoglu, T. Franke, *Lab Chip* **2021**, *22*, 193.
[27] X. Bai, S. Bin, D. Yuguo, Z. Wei, F. Yanmin, C. Yuanyuan, Z. Deyuan, A. Fumihito, F. Lin, *Sens. Actuators, A* **2020**, *315*, 112340.
[28] A. G. Guex, N. D. Marzio, D. Eglin, M. Alini, T. Serra, *Mater Today Bio* **2021**, *10*, 100110.
[29] R. J. Shilton, M. Travagliati, F. Beltram, M. Cecchini, *Adv. Mater.* **2014**, *26*, 4941.
[30] K. Melde, A. G. Mark, T. Qiu, P. Fischer, *Nature* **2016**, *537*, 518.
[31] Z. Ma, Y. Zhou, D. J. Collins, Y. Ai, *Lab Chip* **2017**, *17*, 3176.
[32] R. A. Sahely, J.-C. Gerbedoen, N. Smagin, R. Chutani, O. B. Matar, M. Baudoin, *arXiv* **2022**, 2203.05214.

[33] D. J. Collins, C. Devendran, Z. Ma, J. W. Ng, A. Neild, Y. Ai, *Sci. Adv.* **2016**, *2*, e1600089.

[34] Q. Wang, A. Riaud, J. Zhou, Z. Gong, M. Baudoin, *Phys. Rev. Appl.* **2021**, *15*, 044034.

[35] S. J. Raymond, D. J. Collins, R. O'Rorke, M. Tayebi, Y. Ai, J. Williams, *Sci. Rep.* **2020**, *10*, 8745.

[36] Z. Ma, K. Melde, A. G. Athanassiadis, M. Schau, H. Richter, T. Qiu, P. Fischer, *Nat. Commun.* **2020**, *11*, 4537.

[37] Y. Gu, C. Chen, J. Rufo, C. Shen, Z. Wang, P. H. Huang, H. Fu, P. Zhang, S. A. Cummer, Z. Tian, T. J. Huang, *ACS Nano* **2020**, *14*, 14635.

[38] Z. Ma, Y. Zhou, F. Cai, L. Meng, H. Zheng, Y. Ai, *Lab Chip* **2020**, *20*, 2947.

[39] D. J. Collins, R. O'Rorke, A. Neild, J. Han, Y. Ai, *Soft Matter* **2019**, *15*, 8691.

[40] M. Xu, P. V. S. Lee, D. J. Collins, *Lab Chip* **2021**, *22*, 90.

[41] K.-W. Tung, P.-S. Chung, C. Wu, T. Man, S. Tiwari, B. Wu, Y.-F. Chou, F.-L. Yang, P.-Y. Chiou, *Lab Chip* **2019**, *19*, 3714.

[42] Y. Bian, F. Guo, S. Yang, Z. Mao, H. Bachman, S. Y. Tang, L. Ren, B. Zhang, J. Gong, X. Guo, T. J. Huang, *Microfluid Nanofluidics* **2017**, *21*, 132.

[43] X. Lu, J. Twiefel, Z. Ma, T. Yu, J. Wallaschek, P. Fischer, *Adv. Sci.* **2021**, *8*, 2100888.

[44] X. Lu, Y. Wei, H. Ou, C. Zhao, L. Shi, W. Liu, *Small* **2021**, *17*, 2104516.

[45] C. Zhang, X. Guo, P. Brunet, M. Costalonga, L. Royon, *Microfluid Nanofluidics* **2019**, *23*, 104.

[46] P. H. Huang, N. Nama, Z. Mao, P. Li, J. Rufo, Y. Chen, Y. Xie, C. H. Wei, L. Wang, T. J. Huang, *Lab Chip* **2014**, *14*, 4319.

[47] Y. Zhou, Wang, H. , Ma, Z. , Yang, J. K. W. , Ai, Y. , *Adv. Mater.* **2020**, *5*.

[48] T. Qiu, S. Palagi, A. G. Mark, K. Melde, F. Adams, P. Fischer, *Appl. Phys lett.* **2016**, *109*, 191602.

[49] Y. Zhou, Z. Ma, Y. Ai, *Anal. Chem.* **2020**, *92*, 12795.

[50] M. Tayebi, R. O'Rorke, H. C. Wong, H. Y. Low, J. Han, D. J. Collins, Y. Ai, *Small* **2020**, *16*, 2000462.

[51] X. Lu, A. Martin, F. Soto, P. Angsantikul, J. Li, C. Chen, Y. Liang, J. Hu, L. Zhang, J. Wang, *Adv. Mater. Technol.* **2018**, *4*, 1800374.

[52] R. Rasouli, M. Tabrizian, *Small* **2021**, *17*, e2101931.

[53] L. Feng, B. Song, Y. Chen, S. Liang, Y. Dai, Q. Zhou, D. Chen, X. Bai, Y. Feng, Y. Jiang, D. Zhang, F. Arai, *Biomicrofluidics* **2019**, *13*, 064103.

[54] Z. Wang, P. H. Huang, C. Chen, H. Bachman, S. Zhao, S. Yang, T. J. Huang, *Lab Chip* **2019**, *19*, 4021.

[55] K. Kolesnik, M. Xu, P. V. S. Lee, V. Rajagopal, D. J. Collins, *Lab Chip* **2021**, *21*, 2837.

[56] K. Kolesnik, P. Hashemzadeh, D. Peng, M. E. M. Stamp, W. Tong, V. Rajagopal, M. Miansari, D. J. Collins, *Phys Rev E* **2021**, *104*, 045104.

[57] M. Settnes, H. Bruus, *Phys Rev E Stat Nonlin Soft Matter Phys* **2012**, *85*, 016327.

[58] M. Wiklund, R. Green, M. Ohlin, *Lab Chip* **2012**, *12*, 2438.

[59] C. Bouyer, P. Chen, S. Guven, T. T. Demirtas, T. J. Nieland, F. Padilla, U. Demirci, *Adv. Mater.* **2016**, *28*, 161.

[60] Z. Tian, Z. Wang, P. Zhang, T. D. Naquin, J. Mai, Y. Wu, S. Yang, Y. Gu, H. Bachman, Y. Liang, Z. Yu, T. J. Huang, *Sci. Adv.* **2020**, *6*, eabb0494.

[61] S. Collignon, O. Manor, J. Friend, *Adv. Funct. Mater.* **2017**, *28*, 1704359.

[62] M. B. Dentry, L. Y. Yeo, J. R. Friend, *Phys Rev E Stat Nonlin Soft Matter Phys* **2014**, *89*, 013203.

[63] A. S. Basu, *Lab Chip* **2013**, *13*, 1892.

[64] Z. Ma, A. W. Holle, K. Melde, T. Qiu, K. Poeppel, V. M. Kadiri, P. Fischer, *Adv. Mater.* **2020**, *32*, 1904181.

[65] Z. Chen, P. Liu, X. Zhao, L. Huang, Y. Xiao, Y. Zhang, J. Zhang, N. Hao, *Appl. Mater. Today* **2021**, *25*, 101239.

[66] C. Dillinger, N. Nama, D. Ahmed, *Nat Commun* **2021**, *12*, 6455.

[67] N. F. Laubli, J. T. Burri, J. Marquard, H. Vogler, G. Mosca, N. Vertti-Quintero, N. Shamsudhin, A. deMello, U. Grossniklaus, D. Ahmed, B. J. Nelson, *Nat. Commun.* **2021**, *12*, 2583.

[68] R. P. Simon, T. T. Habe, R. Ries, M. Winter, Y. Wang, A. Fernandez-Montalvan, D. Bischoff, F. Runge, W. Reindl, A. H. Luippold, F. H. Buttner, *SLAS Discov* **2021**, *26*, 961.

[69] D. Petta, V. Basoli, D. Pellicciotta, R. Tognato, J. Barcik, C. Arrigoni, E. D. Bella, A. R. Armiento, C. Candrian, R. G. Richards, M. Alini, M. Moretti, D. Eglin, T. Serra, *Biofabrication* **2020**, *13*, 015004.